

17. Huang, Y. *et al.* Logic gates and computation from assembled nanowire building blocks. *Science* **294**, 1313–1317 (2001).
18. Chen, C.-L. *Elements of Optoelectronics and Fiber Optics* (Irwin, Chicago, 1996).
19. Wang, J., Gudiksen, M. S., Duan, X., Cui, Y. & Lieber, C. M. Highly polarized photoluminescence and polarization sensitive photodetectors from single indium phosphide nanowires. *Science* **293**, 1455–1457 (2001).
20. Bagnall, D. M., Ullrich, B., Sakai, H. & Segawa, Y. Micro-cavity lasing of optically excited CdS thin films at room temperature. *J. Cryst. Growth* **214/215**, 1015–1018 (2000).
21. Bagnall, D. M., Ullrich, B., Qiu, X. G., Segawa, Y. & Sakai, H. Microcavity lasing of optically excited cadmium sulphide thin films at room temperature. *Opt. Lett.* **24**, 1278–1280 (1999).
22. Huang, Y., Duan, X., Cui, Y. & Lieber, C. M. GaN nanowire nanodevices. *Nano Lett.* **2**, 101–104 (2002).
23. Gudiksen, G. S., Lauhon, L. J., Wang, J., Smith, D. & Lieber, C. M. Growth of nanowire superlattice structures for nanoscale photonics and electronics. *Nature* **415**, 617–620 (2002).
24. Lauhon, L. J., Gudiksen, M. S., Wang, D. & Lieber, C. M. Epitaxial core-shell and core-multishell nanowire heterostructures. *Nature* **420**, 57–61 (2002).
25. El Assali, K. *et al.* Some structural and optical properties of CdS thin films prepared by RF sputtering. *Phys. Status Solidi A* **178**, 701–708 (2000).

Supplementary Information accompanies the paper on *Nature's* website
(<http://www.nature.com/nature>).

Acknowledgements We thank H. Park, X. Zhuang & M. S. Gudiksen for helpful discussion. C.M.L. is grateful for support of this work by the Air Force Office of Scientific Research.

Competing interests statement The authors declare that they have no competing financial interests.

Correspondence and requests for materials should be addressed to C.M.L.
(e-mail: cml@cmliris.harvard.edu).

Rapid Cenozoic glaciation of Antarctica induced by declining atmospheric CO₂

Robert M. DeConto* & David Pollard†

* Department of Geosciences, University of Massachusetts, Amherst, Massachusetts 01003, USA

† EMS Environment Institute, The Pennsylvania State University, University Park, Pennsylvania 16802, USA

The sudden, widespread glaciation of Antarctica and the associated shift towards colder temperatures at the Eocene/Oligocene boundary (~34 million years ago) (refs 1–4) is one of the most fundamental reorganizations of global climate known in the geologic record. The glaciation of Antarctica has hitherto been thought to result from the tectonic opening of Southern Ocean gateways, which enabled the formation of the Antarctic Circumpolar Current and the subsequent thermal isolation of the Antarctic continent⁵. Here we simulate the glacial inception and early growth of the East Antarctic Ice Sheet using a general circulation model with coupled components for atmosphere, ocean, ice sheet and sediment, and which incorporates palaeogeography, greenhouse gas, changing orbital parameters, and varying ocean heat transport. In our model, declining Cenozoic CO₂ first leads to the formation of small, highly dynamic ice caps on high Antarctic plateaux. At a later time, a CO₂ threshold is crossed, initiating ice-sheet height/mass-balance feedbacks that cause the ice caps to expand rapidly with large orbital variations, eventually coalescing into a continental-scale East Antarctic Ice Sheet. According to our simulation the opening of Southern Ocean gateways plays a secondary role in this transition, relative to CO₂ concentration.

Antarctica has been located over southern polar latitudes since the

Early Cretaceous⁶, yet is thought to have remained mostly ice-free, vegetated, and with mean annual temperatures well above freezing until the Eocene/Oligocene boundary^{4,7}. Evidence for cooling and the sudden growth of an East Antarctic Ice Sheet (EAIS) comes from marine records (refs 1–3), in which the gradual cooling from the presumably ice-free warmth of the Early Tertiary to the cold ‘icehouse’ of the Late Cenozoic is punctuated by a sudden >1.0‰ rise in benthic δ¹⁸O values at ~34 million years (Myr). More direct evidence of cooling and glaciation near the Eocene/Oligocene boundary is provided by drilling on the East Antarctic margin⁸, the record of circum-Antarctic ice-rafted debris⁹, a shift in the clay composition of circum-Antarctic sediments¹⁰, and the fossil record of Antarctic vegetation¹¹. Glaciation is believed to have begun in the East Antarctic interior, discharging mainly via the Lambert Graben to Prydz Bay, with the Transantarctic Mountains restricting ice flow towards the Ross Sea until the ice sheets became larger in the Middle Oligocene⁴. Palaeogene Antarctic ice sheets appear to have been temperate, highly dynamic^{7,12}, and paced by Milankovitch orbital parameters^{1,13} in much the same way as the Quaternary ice sheets of the Northern Hemisphere.

The initial growth of the EAIS near the Eocene/Oligocene boundary has been attributed to the tectonic opening of ocean gateways between Antarctica and Australia (Tasmanian Passage), and Antarctica and South America (Drake Passage), leading to the organization of the Antarctic Circumpolar Current (ACC) and the ‘thermal isolation’ of Antarctica^{5,14}. This notion is supported by ocean general circulation model (OGCM) simulations, showing that the opening of Drake Passage and the organization of an ACC reduces southward oceanic heat transport and cools Southern Ocean sea surface temperatures (SSTs) by ~3 °C (refs 15, 16). However, although most tectonic reconstructions place the opening of the Tasmanian Passage close to the Eocene/Oligocene boundary, Drake Passage may not have provided a significant deep-water passage until several million years later^{17,18}. Additionally, these OGCM simulations lacked realistic atmospheric components, so the effects on Antarctic climate are unresolved.

Alternatively, declining atmospheric CO₂ may have played a

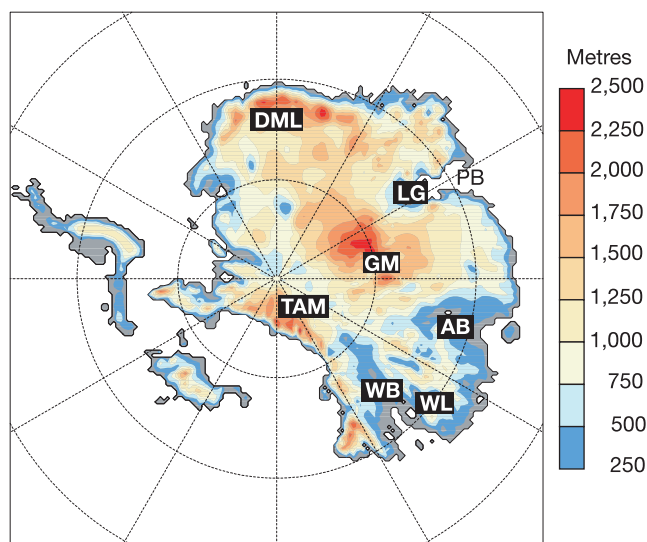


Figure 1 Early Cenozoic ice-free Antarctic topography in metres above sea level. This was reconstructed from a modern 5-km database³⁰, isostatically relaxed to ice-free equilibrium and interpolated to the 40-km polar stereographic grid of the ice-sheet model. Abbreviated place names mentioned in the text are also shown: AB, Aurora Basin; DML, Dronning Maud Land; GM, Gamburtsev Mountains; LG, Lambert Graben; PB, Prydz Bay; TAM, Transantarctic Mountains; WB, Wilkes Basin; WL, Wilkes Land.

fundamental role in Palaeogene cooling and Antarctic glaciation. Most estimates of early Cenozoic CO_2 mixing ratios range between 2 and 5 times present values, falling through the Cenozoic until reaching near-modern values sometime in the Neogene^{19,20}. The cooling due to declining p_{CO_2} would have gradually lowered annual snowline elevations until they intersected extensive regions of high Antarctic topography. Once some threshold was reached, feedbacks related to snow/ice-albedo and ice-sheet height/mass-balance^{21–23} could have initiated rapid ice-sheet growth during orbital periods favourable for the accumulation of glacial ice.

To test the relative importance of changing atmospheric CO_2 , orbital parameters and ocean heat transport in the nucleation and subsequent fluctuations of the early EAIS, we have developed a coupled global climate model (GCM) and dynamic ice-sheet model designed for experiments over long timescales. Previous dynamic ice-sheet models of ancient Antarctic ice sheets have used empirical parameterizations based on modern climates for their surface mass-balance forcing²⁴. Instead, we use the GENESIS (version 2.1) GCM²⁵

with a 50-m slab ocean (see Methods) responding to evolving Palaeogene boundary conditions to provide the meteorological input for our dynamic ice-sheet model experiments. A three-dimensional ice-sheet model of ice dynamics and bedrock response is asynchronously coupled to the GCM, allowing feedbacks between the ice sheet and atmospheric model components, and accounting for cyclical orbital forcing on 10^4 -yr timescales.

Boundary conditions for our Eocene/Oligocene climate/ice-sheet simulations are based on a global 34 Myr palaeogeography, including reconstructions of shorelines, rebounded ice-free topography (Fig. 1) and vegetation. To simulate the growth of Antarctic ice around the Eocene/Oligocene boundary, the GCM–ice-sheet model would ideally be run together through millions of years. However, the computational expense of the GCM makes that infeasible, so we have developed a new two-step scheme (see Methods) accounting for both orbital forcing and a decline in CO_2 , from $4 \times$ to $2 \times$ PAL (preindustrial atmospheric level, taken as 280 parts per million by volume (p.p.m.v.)) over a 10-Myr period.

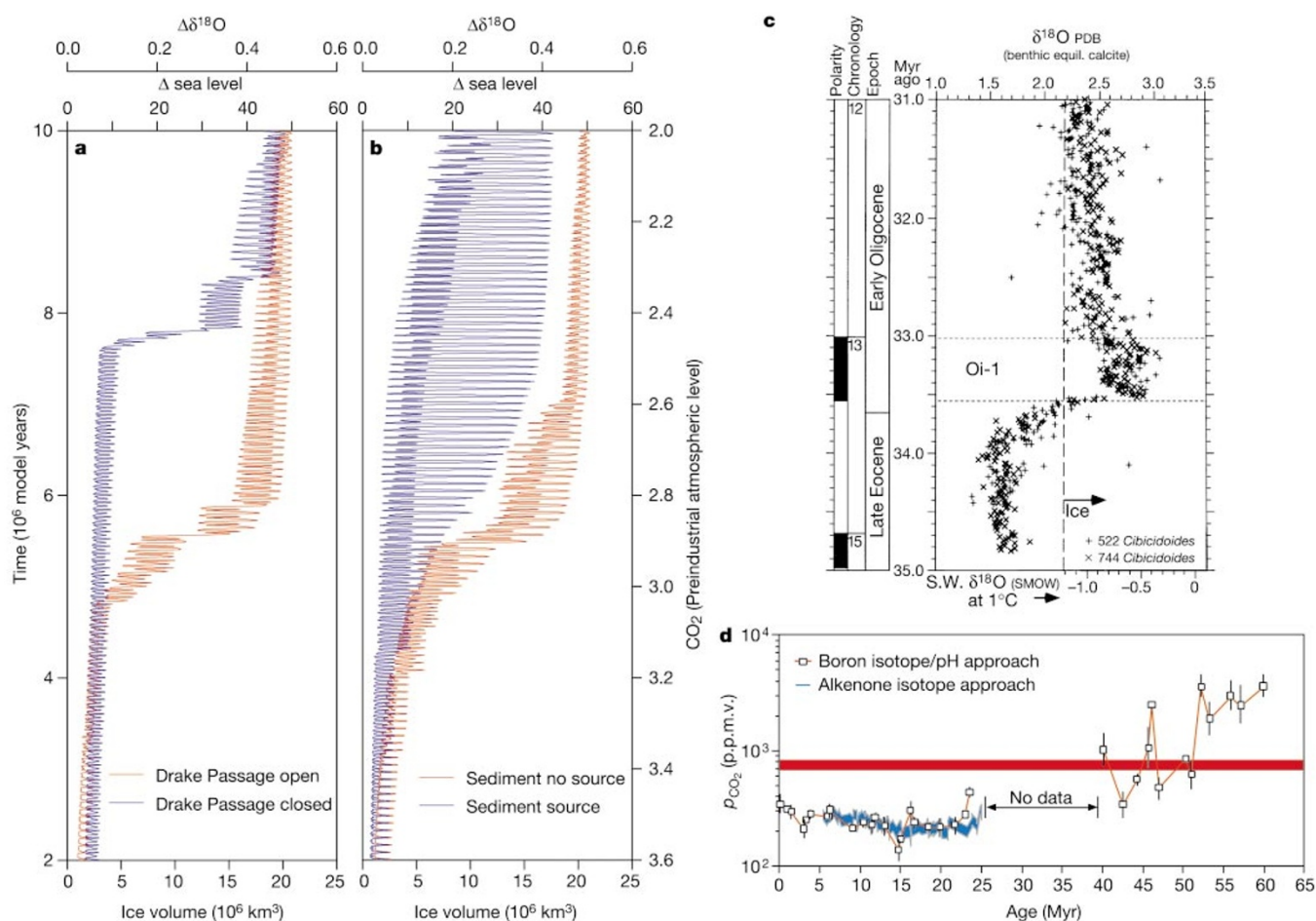


Figure 2 The transient climate-cryosphere response to a prescribed decline in CO_2 from $4 \times$ to $2 \times$ preindustrial atmospheric level over a 10-Myr period. Ice volume, and equivalent changes in sea level (Δ sea level) and the mean isotopic composition of the ocean ($\Delta\delta^{18}\text{O}$) are shown for two pairs of simulations: **a**, red curve, nominal case, representing an open Drake Passage; **a**, blue curve, with the global climate model ocean heat transport coefficient increased in the Southern Hemisphere to represent a closed Drake Passage; **b**, red curve, with deformable sediment added to the ice model and no generation of new till; **b**, blue curve, with the same sediment model but including subglacial generation of new till where basal ice is in contact with clean bedrock. Equivalent sea level changes were calculated according to the global ocean-area fraction in our 34-Myr palaeogeography (0.731). $\Delta\delta^{18}\text{O}$ was calculated assuming a 0.0091

change in $\delta^{18}\text{O}$ per 1-m change of sea level. **c**, High-resolution foraminiferal stable isotope data¹ from Ocean Drilling Program (ODP) sites 522 and 744 are shown for comparison with our simulated glacial transitions in **a** and **b**. The magnitude of the observed Eocene/Oligocene oxygen isotopic excursion is larger than modelled, probably because of the influence of deep-ocean cooling on $\delta^{18}\text{O}$, our assumed constant of proportionality with sea level being too low, and/or the model's lack of significant West Antarctic ice and its buttressing effect on the EAIS. **d**, proxy estimates of p_{CO_2} based on a boron isotope/pH approach¹⁹ and an alkenone isotope approach²⁰ reprinted from ref. 2 with the permission of the American Association for the Advancement of Science for comparison with the critical range of CO_2 values (thick red line) seen in **a** ($1 \times \text{CO}_2 = 280$ p.p.m.v.).

The 10-Myr integrations illustrate the possible evolution of the EAIS and several distinct modes of early ice-sheet variability as p_{CO_2} declined through the Palaeogene. In our nominal experiment (Fig. 2a, red), relatively small, isolated ice caps first form in the highest elevations of Dronning Maud Land in response to orographically lifted maritime moisture, producing high winter snowfall over the high elevations of the Polar Plateau/Gamburtsev Mountain region and along the Transantarctic Mountains (Fig. 3a). However, long-term ice variations are dominated by changes in summer temperatures and melting, not by changes in snowfall. At around $3 \times \text{CO}_2$, a small ice-sheet threshold is reached first for the Gamburtsev ice cap (Fig. 3b), which rapidly expands owing to height/mass-balance feedback^{21,22} during orbital periods with minimal summer insolation. The first significant ice caps are not large enough to reach sea level around much of the coast, but produce orbitally paced changes in ice volume large enough to account for significant variations in eustatic sea level (Fig. 2). Within the next several eccentricity cycles, additional jumps in ice volume occur as the individual ice caps permanently coalesce (Fig. 3c), remaining joined even through warm-summer orbital periods. At $\sim 2.8 \times \text{CO}_2$, the once individual ice caps form a continental-scale EAIS (Fig. 3d). As CO_2 continues to fall, ice-sheet extent becomes limited

more by continental shorelines and not by land-based ablation zones. This truncates the amplitude of the response to orbital forcing and increases ice-sheet stability for the remainder of the simulation (Fig. 2).

In our nominal 10 Myr experiment, the Drake and Tasman passages were effectively assumed to be open. To address the importance of the opening of Southern Ocean gateways on EAIS mass-balance, we adjusted our model to reflect changes found in previous OGCM sensitivity studies with an open versus closed Drake Passage^{15,16}. In these studies, a closed Drake Passage increases southward ocean heat transport by 15–20% over all southern latitudes. To mimic that effect while retaining the computational efficiency of a slab ocean, we adjusted the slab diffusion coefficient so as to increase ocean heat transport by 20% over the same latitudes, and repeated the 10-Myr experiment.

The two 10-Myr experiments in Fig. 2a have a permanently closed or open Drake Passage, allowing the effect on the timing of the CO_2 -induced transition to be seen clearly. The parameterized opening of Drake Passage has a significant effect on ice volume only when CO_2 values are within the critical range: $\sim 2.5 \times$ to $3 \times$ present. With Drake Passage closed, the transition to major glaciation is delayed until CO_2 falls an additional ~ 140 p.p.m.v. compared with that

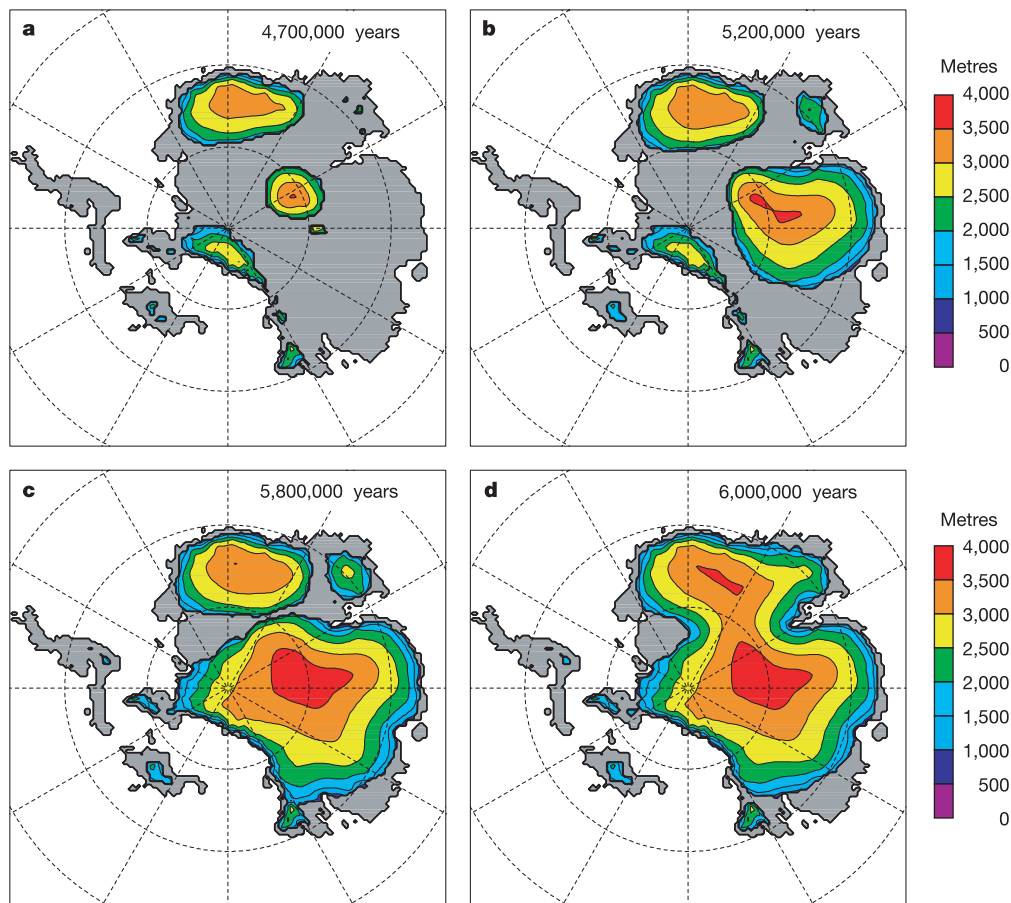


Figure 3 Ice-surface elevations at instantaneous times during the transition from ‘Greenhouse’ to ‘Icehouse’ conditions in our nominal 10-Myr simulation (Fig. 2a, red curve). **a**, At year 4,700,000, three small, isolated ice caps exist on the highest elevations of Dronning Maud Land and the Gamburtsev and Transantarctic mountains, fluctuating only slightly with orbital variations. **b**, At year 5,200,000 as CO_2 declines below $3 \times$ preindustrial atmospheric level, a small ice-sheet threshold^{21,22} has been reached for the Gamburtsev ice cap, which greatly expands in volume. **c**, At year 5,800,000, further decline of CO_2 allows the Gamburtsev and Transantarctic ice caps to coalesce

permanently, buttressing each other to form a much larger central ice sheet. This central ice cap makes repeated, but temporary, contact with the Dronning Maud Land ice cap during orbital periods with minimal summer insolation. **d**, By year 6,000,000, a further jump in volume occurs as the Dronning Maud ice cap permanently coalesces with the rest of the ice mass, forming a continental-scale East Antarctic Ice Sheet with two main spreading centres and major discharges down the Lambert Graben and other bedrock troughs to Prydz Bay and the Wilkes and Aurora basins.

when Drake Passage is open. Thus, a 20% change in southward oceanic-heat convergence has a significant effect on the timing of glacial inception, but only within a relatively narrow range of CO_2 (Fig. 2). If Drake Passage opened outside this range of heightened cryosphere sensitivity, the effect would be small. If the opening occurred at levels of CO_2 greater than $\sim 3 \times$ present, a continental ice sheet would not have formed. If the opening of Drake Passage occurred after 34 Myr ago, as suggested by geologic evidence¹⁸, then the EAIS ice sheet already in existence would have become only slightly larger.

Another 10-Myr simulation was done with the addition of a subglacial deforming sediment component in the ice-sheet model. Subglacial processes are thought to be important for the behaviour of fast-moving West Antarctic ice streams²⁶ and the evolution of Northern Hemisphere Quaternary ice sheets²⁷. The sediment model²⁷ accounts for extra sliding within a sediment layer of variable thickness, and predicts the evolving continental-scale distribution of till (see Methods). The addition of sediment in the 10-Myr integration (Fig. 2b, red) results in enhanced orbital variability, especially around the major transition, but it does not significantly affect the transition's timing. The enhanced variability is caused by thinner ice-sheet profiles and wider ablation zones, as found for Quaternary ice sheets of the Northern Hemisphere²⁷. After the transition, the ice sheets eventually revert to the behaviour of the non-sediment model, after easily eroded sediment in the continental interior is scraped clean by repeated cycles. When the sediment model is modified to include subglacial generation of new till (see Methods), considerable amounts of sediment are maintained under the ice and the orbital variability remains much larger through most of the simulation (Fig. 2b, blue). Compared with proxy records influenced by ice volume across the Eocene/Oligocene boundary (Fig. 2c), the simulations with no till generation (Fig. 2b, red) or no sediment at all (Fig. 2a, red) appear more realistic. However, this simple representation of continental-scale sediment is intended only to illustrate the possible envelope of effects on Antarctic ice evolution.

In summary, our model results provide an alternative explanation for the sudden build-up and subsequent variations of Antarctic ice near the Eocene/Oligocene boundary, emphasizing atmospheric CO_2 , orbital forcing, and ice-climate feedbacks as the primary causes of the Eocene/Oligocene climate transition. As CO_2 declined through the Palaeogene, the gradual lowering of the Antarctic snowline began intersecting areas of high topography, first producing small, isolated ice caps. As CO_2 continued to fall, height/mass-balance feedbacks were initiated suddenly, producing larger dynamic ice sheets that alternately coalesced and separated in response to orbital forcing. With further decline of CO_2 , a single, large EAIS became a more permanent feature, almost insensitive to orbital forcing, with very little summer melting, and accumulation zones reaching sea-level around most of the continent. Although the rate of CO_2 decline used in our model is only 56 p.p.m.v. per million years, it does produce a rather sudden climatic transition due to the initiation of internal climate system feedbacks. These results are in good agreement with high-resolution benthic $\delta^{18}\text{O}$ and Mg/Ca data spanning the Eocene/Oligocene boundary (refs 1 and 3) (Fig. 2c) and the sudden occurrence of ice-rafted debris in the Southern Ocean⁹. Although the simulated CO_2 /ice-sheet initiation threshold (between $3 \times$ and $2.5 \times$ PAL) may be model dependent, it is within the general range of proxy estimates of mid-Cenozoic p_{CO_2} (refs 19 and 20) (Fig. 2d).

The opening of Southern Ocean gateways and the formation of the ACC undoubtedly cooled high southern latitudes. However, the simulated effect of a 20% change in ocean heat transport associated with the opening of Drake Passage is shown to have a smaller effect than that expected in the transition from a 'greenhouse' to an 'icehouse' climate. In our model, the opening of Drake Passage can only be a potential trigger for glacial inception when atmospheric

CO_2 is within a relatively narrow range (Fig. 2a, d), reinforcing the importance of p_{CO_2} as a fundamental boundary condition for Cenozoic climate change. More explicit modelling of changes in ocean circulation using coupled atmospheric-oceanic GCMs, along with more proxy estimates of Palaeogene CO_2 around the Eocene/Oligocene boundary, will help to reveal the relative role of climate-forcing factors on Cenozoic Antarctic glaciation. □

Methods

Global climate model

The atmospheric component of GENESIS version 2.1 has 18 vertical layers and a spectral resolution of T31 ($\sim 3.75^\circ \times 3.75^\circ$), coupled to $2^\circ \times 2^\circ$ surface models including a non-dynamic 50-m slab ocean, a dynamic-thermodynamic sea-ice model, and multi-layer models of soil, snow and vegetation. Ocean heat transport is not prescribed, but is calculated as linear diffusion down the local ocean-temperature gradient, with the coefficient depending on latitude and the zonal fraction of land versus sea. Modifications to the standard GENESIS version 2.0 (ref. 25) include an improved slab diffusion coefficient, which yields realistic present zonal ocean heat transport.

Ice-sheet model

The thermo-mechanical ice-sheet model is based on the vertically integrated continuity equation for ice mass (refs 24 and 29), using a $40 \text{ km} \times 40 \text{ km}$ polar stereographic grid. The evolution of ice geometry is determined by surface mass balance, basal melting, and ice flow. Ice temperatures are predicted to account for their effect on rheology and basal sliding. The local bedrock response to ice load is a simple relaxation towards isostasy, with a time constant of 5,000 years. Lithospheric flexure is modelled by linear elastic deformation²⁸. Ice shelves are not included, and ice extent is constrained by continental shorelines. This ignores sea-level change and inhibits the formation of a marine-based West Antarctic Ice Sheet, which will be addressed in future work.

Deforming sediment model

The sediment component added to the ice-sheet model accounts for extra sliding due to horizontal shear in a layer of subglacial sediment, driven by the basal shear stress of the ice. The most appropriate sediment rheology is controversial²⁶; we use a slightly nonlinear rheology²⁷, extended here to two horizontal dimensions. This allows significant shear in the upper tens of centimetres to approximately 1 m of sediment below the ice, with deformation occurring only where the basal temperature is at the pressure melting point and the sediment is saturated. Our 10-Myr simulations are initialized with a uniform 50 m layer of regolith, assumed to have accumulated before the onset of major glaciation. Two simple parameterizations are added to simulate the long-term continental-scale evolution of sediment: (1) ice-free transport of moraines by rivers, modelled as instantaneous fluvial transport down the topographic gradient to the coast, lakes, or ice dams; and (2) subglacial generation of new till, proportional to the work done by basal sliding where the existing sediment is thin or non-existent.

Global climate model/ice-sheet coupling

Relevant monthly mean meteorological fields used in the calculation of net annual surface-ice mass balance (surface air temperature and precipitation) are horizontally interpolated from the GCM to the much finer ice-sheet grid. Temperatures are lapse-rate adjusted to account for the GCM's coarse representation of topography²⁵. A computationally economical positive degree-day parameterization with an imposed diurnal cycle is used to calculate accumulation and ablation from the monthly mean temperatures and precipitation²⁹, including a correction for refreezing of meltwater²⁵. Mass balance is re-computed every 200 years to account for changing ice elevations.

First step of long-term integrations

To perform long (10^6 yr) ice-sheet simulations and still make use of GCM climate solutions, we use a two-step asynchronous coupling scheme. In the first step, relatively short, 40 kyr simulations are performed with varying orbital parameters but fixed CO_2 . A synthetic orbital sequence is used (see Supplementary Information), with periodicities that are exact multiples or divisors of 40 kyr; that is, precession, obliquity and eccentricity vary sinusoidally with periods of 20 kyr, 40 kyr and 80 kyr, respectively. This captures the essence of orbital forcing. In each 40-kyr run, the ice-sheet model is integrated continuously, starting with no ice. The GCM is run for a few decades at the start of each simulation, and again every 10 kyr with updated ice-sheet size and orbit parameters to provide continuous mass balance for the ice model. Monthly mean temperatures and precipitation from the last 10 yr of each of the five GCM snapshots are stored for later use. Four 40-kyr sequences were conducted, with fixed CO_2 levels of $2 \times$ and $3 \times$ PAL, with and without a GCM modification representing Drake Passage closure (see text).

Second step of long-term integrations

The ice-sheet model is driven continuously for 10 million years, computing mass balances every 200 years from the appropriate linear weights of the stored sets of monthly GCM climates from the first step. The same synthetic 40-kyr orbital sequence is repeated in alternating forward and backward passes, to produce a smooth 80-kyr eccentricity cycle. The ice-driving climatology is linearly weighted in time between the two surrounding orbital GCM solutions. In addition, a steady decline in atmospheric CO_2 is specified, from $4 \times$ to $2 \times$ PAL over 10 Myr, by interpolating/extrapolating with respect to CO_2 level

between the appropriate GCM climates and accounting for the logarithmic radiative effect of CO₂. Unlike the shorter 40-kyr simulations (first step), ice albedo and topographic feedbacks are not calculated explicitly, but the latter are captured by the lapse-rate correction in the mass-balance calculations.

Received 25 July; accepted 12 November 2002; doi:10.1038/nature01290.

1. Zachos, J. C., Quinn, T. M. & Salamy, K. A. High-resolution (10⁴ years) deep-sea foraminiferal stable isotope records of the Eocene–Oligocene climate transition. *Paleoceanography* **11**, 251–266 (1996).
2. Zachos, J., Pagani, M., Sloan, L. & Thomas, E. Trends, rhythms, and aberrations in global climate 65 Ma to present. *Science* **292**, 686–693 (2001).
3. Lear, C. H., Elderfield, H. & Wilson, P. A. Cenozoic deep-sea temperatures and global ice volumes from Mg/Ca in benthic foraminiferal calcite. *Science* **287**, 269–272 (2000).
4. Barrett, P. J. Antarctic paleoenvironment through Cenozoic times—a review. *Terr. Antarct.* **3**, 103–119 (1996).
5. Kennett, J. P. Cenozoic evolution of Antarctic glaciation, the circum-Antarctic oceans and their impact on global paleoceanography. *J. Geophys. Res.* **82**, 3843–3859 (1977).
6. Lawver, L. A., Gahagan, L. M. & Coffin, M. F. in *The Antarctic Paleoenvironment: A Perspective on Global Change* (eds Kennett, J. P. & Warnke, D. A.) 7–30 (American Geophysical Union, Washington DC, 1992).
7. Hambrey, M. J., Larsen, B. & Ehrmann, W. U. in *Ocean Drilling Program Scientific Results 119* (eds Barron, J. & Larsen, B.) 77–132 (College Station, Texas, 1991).
8. Wilson, G. S., Roberts, A. P., Verosub, K. L., Florindo, F. & Sagnotti, L. Magnetobiostratigraphic chronology of the Eocene–Oligocene transition in the CIROS-1 core, Victoria Land margin, Antarctica: Implications for Antarctic glacial history. *Geol. Soc. Am. Bull.* **110**, 35–47 (1998).
9. Zachos, J. C., Breza, J. R. & Wise, S. W. Early Oligocene ice sheet expansion on Antarctica: stable isotope and sedimentological evidence from Kerguelen Plateau, southern Indian Ocean. *Geology* **20**, 569–573 (1992).
10. Ehrmann, W. U. & Mackensen, A. Sedimentologic evidence for the formation of an East Antarctic ice sheet in Eocene/Oligocene time. *Palaeogeogr. Palaeoclimatol. Palaeoecol.* **93**, 85–112 (1992).
11. Francis, J. E. Evidence from fossil plants for Antarctic Paleoclimates over the past 100 million years. *Terr. Antarct. Rep.* **3**, 43–52 (1999).
12. Barrett, P. J., Elston, D. P., Harwood, D. M., McKelvey, B. C. & Webb, P.-N. Mid-Cenozoic record of glaciation and sea-level change on the margin of Victoria Land basin, Antarctica. *Geology* **15**, 634–637 (1987).
13. Naish, T. R. *et al.* Orbitally induced oscillations in the East Antarctic ice sheet at the Oligocene/Miocene boundary. *Nature* **413**, 719–723 (2001).
14. Exon, N., Kennett, J., Malone, M. & the Leg 189 Shipboard Scientific Party. The opening of the Tasmanian gateway drove global Cenozoic paleoclimatic and paleoceanographic changes: results of Leg 189. *JOIDES J.* **26**, 11–17 (2000).
15. Toggweiler, J. R. & Bjornsson, H. Drake Passage and paleoclimate. *J. Quat. Sci.* **15**, 319–328 (2000).
16. Nong, G. T., Najjar, R. G., Seidov, D. & Peterson, W. Simulation of ocean temperature change due to the opening of Drake Passage. *Geophys. Res. Lett.* **27**, 2689–2692 (2000).
17. Lawver, L. A. & Gahagan, L. M. in *Tectonic Boundary Conditions for Climate Reconstructions* (eds Crowley, T. J. & Burke, K. C.) 212–223 (Oxford Univ. Press, New York, 1998).
18. Barker, P. F. & Burrell, J. The opening of Drake Passage. *Mar. Geol.* **25**, 15–34 (1977).
19. Pearson, P. N. & Palmer, M. R. Atmospheric carbon dioxide over the past 60 million years. *Nature* **406**, 695–699 (2000).
20. Pagani, M., Arthur, M. A. & Freeman, K. H. Miocene evolution of atmospheric carbon dioxide. *Paleoceanography* **14**, 273–292 (1999).
21. Birchfield, G. E., Weertman, J. & Lunde, A. T. A model study of the role of high latitude topography in the climatic response to orbital insolation anomalies. *J. Atmos. Sci.* **39**, 71–87 (1982).
22. Abe-Ouchi, A. & Blatter, H. On the initiation of ice sheets. *Ann. Glaciol.* **18**, 203–207 (1993).
23. Maqueda, M., Willmott, A. J., Bamber, J. L. & Darby, M. S. An investigation of the small ice cap instability in the Southern Hemisphere with a coupled atmosphere–sea ice–ocean–terrestrial ice model. *Clim. Dyn.* **14**, 329–352 (1998).
24. Huybrechts, P. Glaciological modelling of the late Cenozoic East Antarctic ice sheet: stability or dynamism? *Geograf. Annal.* **75**, 221–238 (1993).
25. Thompson, S. L. & Pollard, D. Greenland and Antarctic mass balances for present and doubled atmospheric CO₂ from the GENESIS Version-2 Global Climate Model. *J. Clim.* **10**, 871–900 (1997).
26. Kamb, B. in *The West Antarctic Ice Sheet: Behaviour and Environment* (eds Alley, R. A. & Bindshadler, R. A.) 157–199 (American Geophysical Union, Washington DC, 2001).
27. Clark, P. U. & Pollard, D. Origin of the mid-Pleistocene transition by ice-sheet erosion of regolith. *Paleoceanography* **13**, 1–9 (1998).
28. Brothie, J. F. & Sylvester, R. On crustal flexure. *J. Geophys. Res.* **74**, 5240–5252 (1969).
29. Ritz, C., Fabre, A. & Letreguilly, A. Sensitivity of a Greenland ice-sheet model to ice flow and ablation parameters: consequences for the evolution through the last climate cycle. *Clim. Dyn.* **13**, 11–24 (1997).
30. Bamber, J. A. & Bindshadler, R. A. An improved elevation dataset for climate and ice-sheet modelling: validation with satellite imagery. *Ann. Glaciol.* **25**, 439–444 (1997).

Supplementary Information accompanies the paper on Nature's website (<http://www.nature.com/nature>).

Acknowledgements This material is based upon work supported by the National Science Foundation.

Competing interests statement The authors declare that they have no competing financial interests.

Correspondence and requests for materials should be addressed to R.D. (e-mail: deconto@geo.umass.edu).

Evolution of the Archaean crust by delamination and shallow subduction

Stephen F. Foley*, Stephan Buhre† & Dorrit E. Jacob*

* Institut für Geologische Wissenschaften, Universität Greifswald, F.L.-Jahnstrasse 17a, 17487 Greifswald, Germany

† Institut für Mineralogie, Universität Frankfurt, Senckenberganlage 28, 60054 Frankfurt-am-Main, Germany

The Archaean oceanic crust was probably thicker than present-day oceanic crust owing to higher heat flow and thus higher degrees of melting at mid-ocean ridges¹. These conditions would also have led to a different bulk composition of oceanic crust in the early Archaean, that would probably have consisted of magnesium-rich picrite (with variably differentiated portions made up of basalt, gabbro, ultramafic cumulates and picrite). It is unclear whether these differences would have influenced crustal subduction and recycling processes, as experiments that have investigated the metamorphic reactions that take place during subduction have to date considered only modern mid-ocean-ridge basalts^{2,3}. Here we present data from high-pressure experiments that show that metamorphism of ultramafic cumulates and picrites produces pyroxenites, which we infer would have delaminated and melted to produce basaltic rocks, rather than continental crust as has previously been thought. Instead, the formation of continental crust requires subduction and melting of garnet-amphibolite⁴—formed only in the upper regions of oceanic crust—which is thought to have first occurred on a large

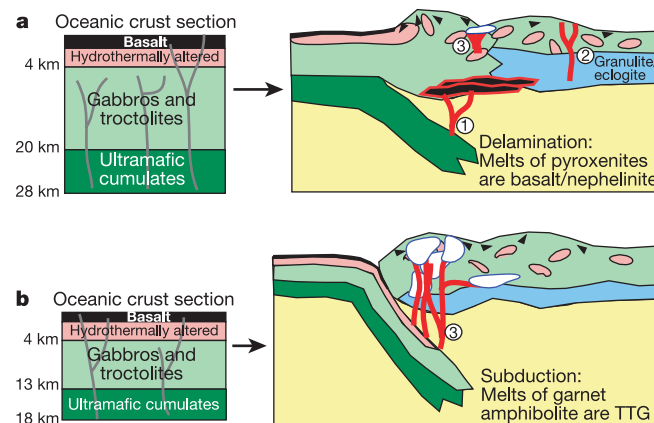


Figure 1 Model for the constitution and fate of oceanic crust. **a**, Hadean/early Archaean; delamination of ultramafic cumulates occurs. **b**, Late Archaean; subduction of the whole ocean crust occurs. Oceanic crust sections are estimated on the basis of eclogite xenolith petrology and chemistry^{12–14}, and thermodynamic modelling of the fractionation of picrites¹⁵. Parental picrites fractionate at the crust–mantle boundary to produce about 30% ultramafic cumulates, predominantly olivine and clinopyroxene. Grey lines indicate that more picritic melts are thought to have approached the surface in the Archaean^{13,16}. Melts may be produced by three main processes: in the Hadean and early Archaean, the metamorphosed ultramafic cumulates (now pyroxenites—see Fig. 2c) delaminate and melt to produce basaltic to nephelinitic melts which are greatly different from early continental crust (process 1). The lower crust may melt as eclogite¹⁰ (process 2), but only after removal of the lower ultramafic cumulate layer. The production of melts from garnet-amphibolites (process 3) is needed to produce continental-crust-like TTG suite⁴; this must have been rare (although not absent) in the early Archaean before the subduction of the hydrothermally altered uppermost basaltic crustal layer, but became important once the whole crust could be subducted²⁰.